JOURNAL OF MATERIALS SCIENCE 29 (1994) 4436–4446

Characterization of glass-ceramic to metal bonds

I. A. ASHCROFT*, B. DERBY
Department of Materials, University of Oxford, Parks Road, Oxford, OXI 3PH, UK

Glass-ceramic thick films were deposited on copper and copper/invar/copper substrates by screen printing and subsequent firing in a belt furnace. One lithium–zinc silicate glass and two lithium–aluminosilicate glasses were deposited. Microstructures of the coatings and the coating/substrate interfaces were studied using optical and electron optical techniques. SEM was used to investigate the glass-ceramic microstructure and EPMA to characterize chemical composition across the interface. Crystalline phases were identified using X-ray and electron diffraction. The lithium–aluminosilicate glass-ceramics were composed of lithium disilicate, β-spodumene and quartz crystals in residual glass. Lithium disilicate and quartz were the only crystals identified in the lithium–zinc silicate glass-ceramic. In all the samples copper diffused extensively through the glass-ceramic during firing and formed Cu_2O precipitates in the glass-ceramics adjacent to the interface. Strong adhesion between the glass-ceramic and the substrates is promoted by copper diffusion and oxide development at the glass-ceramic/substrate interface. The strongest bonds develop when the Cu_2O forms as discrete particles rather than a continuous layer at the interface. Interfacial residual stress also influences the measured adhesion strength.

1. Introduction

Glasses and ceramics are used to coat metals in many applications to give the metal oxidation or corrosion resistance, or to provide thermal or electrical insulation. In the electronics industry ceramic coatings are of particular interest because of the increased use of ceramic packaging. Improvements in microelectronics require increased density, reliability and performance of integrated circuit design, which in turn demands higher-performance substrates, particularly in terms of dielectric properties and heat dissipation. Laminated or composite substrates are often needed to provide the required properties and in many cases metal/ceramic composite substrates are used.

There are a number of advantages to be gained in using glass-ceramics when bonding to metals. First, the component may be fabricated prior to crystallization of the glass thus enabling flexible glass forming and sealing techniques to be used at relatively low temperatures. A low-viscosity glass will flow over the metal surface ensuring intimate contact and promoting bond development. On crystallization the superior properties of a ceramic can be obtained. Second, by careful selection of the parent glass composition and control of the heat treatment during the firing cycle, the phases developed during crystallization may be engineered to achieve a close thermal expansion match with the substrate metal. This reduces the development of residual stresses at the interface which may have a detrimental effect on coating adhesion and reduce its thermal shock resistance. The precise properties of the devitrified glass will depend on the nature and distribution of the crystal phases developed. The adhesion strength of these substrates will depend on the interface microstructures and any segregation of components in the glass-ceramic. Glass-ceramic coating technology has now advanced sufficiently to enable strongly adherent coatings to be deposited onto a variety of metal substrates, either directly or via the use of glass frit or metal braze intermediary layers [1, 2]. However, the microchemistry at the metal/glass-ceramic interface, the mechanisms of adhesion and the influence of the interface and metal diffusion on the crystallization of the glass-ceramic are still poorly understood in many cases.

In the present study thick films of lithium–zinc silicate (LZS) and lithium–aluminosilicate (LAS) glass-ceramics, of thickness ranging from 20 to 200 μm, were deposited on copper and copper/invar/copper laminate. These glass-ceramics have a wide range of potential coating applications because of the large number of possible crystal phases available after heat treatment. The microchemistry of the interfaces in these materials has been studied in order to determine the effects of glass composition, thermal expansion match and substrate pre-treatment on the glass-ceramic microstructure and adhesion at the interface. A number of techniques including electron microscopy, electron probe microanalysis and X-ray diffraction spectroscopy were used to determine the

---

* Now at Department of Materials Engineering, University of Wollongong, Australia.

0022-2461

nature and distribution of phases at the interface. This microstructural information was used to interpret the coating adhesion behaviour.

2. Experimental details

2.1. Experimental materials

Three glass compositions *A*, *C* and *D*, were used and are given in Table I. Glass *A* is of LZS composition whereas *C* and *D* are from the LAS system. P_2O_5 is present as a nucleating agent in all compositions; glass *C* also contains TiO_2 in this role. The glasses were made by mixing and dispersing the constituent oxides in powder form using ball-milling. The mixed powders were melted in a platinum crucible and heated to approximately 1350 °C for 1–2 h. The glass was then quenched in cold water to produce a frit. The dried frit was then ball-milled for approximately 16 h and the resulting powder graded with a 200 mesh (< 75 μm) prior to screen printing.

Oxygen-free copper and a copper/invar/copper laminate (CIC) were used for the substrate materials. The copper was high-conductivity grade (BS1861, 99.5% Cu minimum) and supplied in sheets 750 μm long and 2.6 mm thick. The CIC laminate was supplied by Texas Instruments Ltd. The invar was 170 μm thick and clad with 150 μm copper coatings on each face. The CIC was heated to 960 °C in a nitrogen atmosphere prior to screen printing in order to remove oxygen from the copper. If this was not done blistering occurred at the interface during firing because of oxygen emission. Some of the CIC substrates were subjected to a prior oxidation treatment in which a thin coating of Cu_2O was developed at 960 °C in a controlled atmosphere. This was done in order to gain an understanding of the adhesion-promoting role of any oxide at the interface. Prior to screen printing, both substrates were etched in 50% nitric acid for 30 s followed by ultrasonic cleaning with acetone to ensure a good surface prior to coating.

The glass powder was mixed with an organic binder (ethyl cellulose and butyl cellulose acetate) to form an ink suitable for screen printing. Conventional screen printing techniques were used to coat the metal substrates with a uniform layer of glass. In most cases the glass was deposited onto an approximately 50 mm square of substrate with a 120 mesh stainless steel screen. The film thickness depends on the binder/glass powder mix, the screen mesh size, the number of prints and on the printing operation itself. After depositing each layer of glass, the printing ink was dried in an oven.

TABLE I Parent glass compositions

Glass	*A*	*C*	*D*
SiO_2	75.1	67.4	72.4
Al_2O_3	–	9.5	5.3
ZnO	4.5	0.4	1.5
Li_2O	12.0	11.2	12.9
P_2O_5	1.9	2.3	2.5
TiO_2		1.5	–
B_2O_3	4.0	2.6	3.2
K_2O	2.5	1.7	2.1
MgO	–	1.1	–
BaO	–	1.8	–
ZrO_2	–	0.4	–

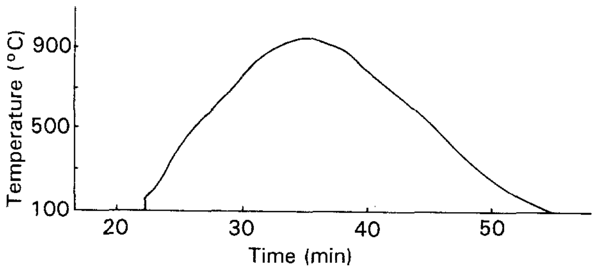

Figure 1 Time/temperature profile for the firing sequence used in the belt furnace for the production of glass-ceramic thick films.

TABLE II Details of the experimental samples

Sample no.	Substrate	Pretreatment	Glass-ceramic	Coating thickness (μm)
3	CIC	Ox	*C*	71
4	CIC	HT	*D*	125
5	Cu	Et	*A*	125
6	Cu	Et	*A*	111
7	CIC	HT	*C*	26
13	CIC	HT	*C*	99
14	Cu	Et	*A*	120
15	CIC	HT	*D*	52
16	Cu	Et	*A*	50
18	CIC	Ox	*C*	96
20	CIC	Et	*A*	122
24	Cu	Et	*A*	155
25	Cu	Et	*A*	215
26	CIC	HT	*D*	126
27	CIC	HT	*D*	200

Et, Etch in 50% nitric acid for 1 min; HT, heat-treated at 960 °C in N_2 atmosphere; Ox, heat-treated at 960 °C with controlled air intake.

The printed substrates were passed through a controlled heat treatment in a belt furnace, the details of which were dependent on the glass-ceramic used. The furnace comprised an entry zone followed by the furnace chamber which is divided into six independently controlled heating zones, followed by an insulated pre-cooling and a water-cooled section. Nitrogen curtains at the entry exit and within the furnace isolate each stage of a complex firing cycle. The firing sequence is illustrated in the temperature profile of Fig. 1. Binder burn-off occurs in a controlled air flow which also allows for some oxidation of the copper surface. This oxidation step was found to be important in controlling the level of adhesion. As the temperature increases the glass softens, melts and flows, wetting the metal surface. Subsequent heat treatment is designed to promote crystallization of the glass-ceramic. The details of all the samples prepared in this study are given in Table II.

2.2. Experimental techniques

X-ray diffraction (XRD) was carried out using CuK_α radiation (0.1542 nm) in a diffractometer with maximum angular (2θ) resolution of $1/4° s^{-1}$. Four sets of samples were used: (i) the surfaces of coated samples were examined *in situ* to identify the crystalline phases present; (ii) selected delaminated coatings were finely ground in a mortar and pestle and the resulting powder analysed (the XRD trace was compared with that of the coating to look for surface effects in the coating); (iii) bulk glass-ceramic materials were studied to investigate the influence of the coating process; and (iv) powdered bulk glass-ceramics were also investigated.

Cross-sections of the coated metal substrates were made using a low-speed diamond saw and these were mounted and polished using conventional techniques for optical microscopy. These sections were used to investigate coating microstructures and measure coating thickness. The coatings were also studied using scanning electron microscopy (SEM) after carbon coating to prevent charging. The sections were also analysed using a dedicated electron microprobe fitted with both energy-dispersive and wavelength-dispersive crystal detectors (EDS and WDS), the latter being used for quantitative analysis. Accelerating voltages of 15 and 20 kV were used. ZAF corrections were used with respect to element and compound standards as appropriate. However, it proved impossible to detect O and Li quantitatively using these techniques, both major constituents of the glass-ceramics used.

Microstructures were also investigated using transmission electron microscopy (TEM). Specimens were made from bulk glass-ceramic samples, cross-sections across the interface and plan views produced by back-thinning. In all cases a combination of mechanical polishing, dimpling a selected area and final ion beam-milling was used to prepare thin sections for examination. In most cases it proved exceptionally difficult or impossible to prepare suitable cross-sections for TEM investigations. Most specimens of the thick films were produced by back-thinning 2–2.5 mm squares of the material as illustrated in Fig. 2. Most of the metal was removed by polishing using 14 μm diamond paste. The remainder of the metal was removed using a flattening tool on the dimpler. When sufficient substrate had been removed the sample was dimpled from both sides using 3 and 1 μm diamond pastes to form a crater. The specimens, dimpled to perforation, were then ion-milled.

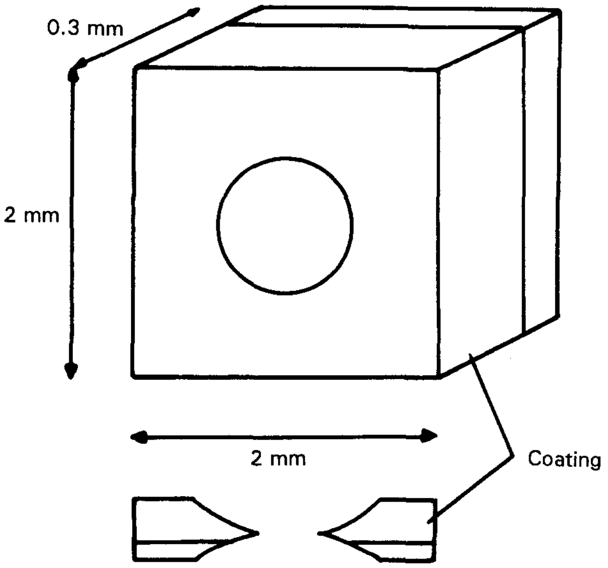

Figure 2 Back-thinning technique used to produce TEM specimens of thick-film samples.

Crystallization sequences in the bulk glass-ceramics were studied using differential thermal analysis. Glass-ceramic specimens were studied using an alumina reference sample.

3. Results

3.1. Crystal phase development

A summary of the XRD data is presented in Table III. α-quartz and lithium disilicate were found in most of the samples examined. β-spodumene was detected in all the LAS samples. Quartz was the major phase present in glass-ceramic *A* and a minor phase in the other samples. No lithium disilicate was identified in the glass-ceramic C/CIC sample despite the bulk glass-ceramic showing the presence of this phase strongly. Comparisons between the order of peak intensities observed here and those recorded in the ASTM powder diffraction files showed some discrepancies, especially for lithium disilicate. However there were no systematic differences with specimen type and thus no effect of texture in the coated films could be determined.

A few peaks in most of the XRD profiles could not be attributed to α-quartz, lithium disilicate or β-spodumene. However there was never sufficient data to positively identify any of the other phases which may be present in these compositions.

Fig. 3 shows the DTA traces from samples of glass *A* and glass *D* heated at 25 °C min^{-1}. This is close to

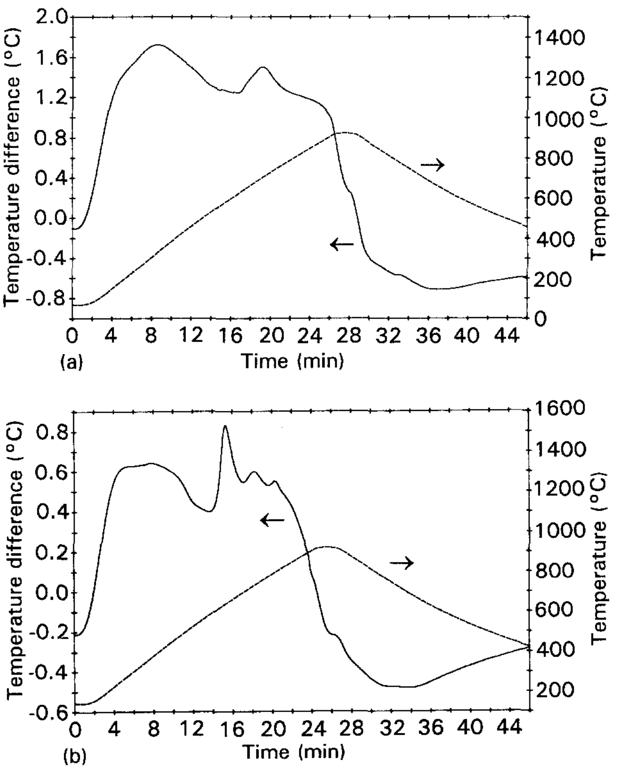

Figure 3 DTA traces from glass-ceramic samples using a thermal cycle similar to that of the belt furnace: (a) glass *A*, (b) glass *D*.

TABLE III Crystalline phases present in glass-ceramic samples

XRD sample (substrate/glass-ceramic)	Crystalline phases detected (in decreasing order of intensity of main reflection)
Copper/*A*	Quartz and lithium disilicate
CIC/*A*	Quartz and lithium disilicate
Powdered coating *A*	Lithium disilicate and quartz
Bulk *A*	Quartz and lithium disilicate
Powdered bulk *A*	Lithium disilicate and quartz
CIC/*C*	β-spodumene and quartz
Bulk *C*	β-spodumene, lithium disilicate and quartz
Powdered bulk *C*	β-spodumene, lithium disilicate and quartz
CIC/*D*	Lithium disilicate, β-spodumene and quartz
Bulk *D*	β-spodumene, lithium disilicate and quartz
Powdered bulk *D*	β-spodumene, lithium disilicate and quartz

the heating rate in the belt furnace. An exothermic peak is visible at 710 °C with glass *A*. Both glasses *C* and *D* showed very similar traces with peaks at 640 °C, 740 °C and 800 °C. These results are consistent as both glasses *C* and *D* have similar LAS compositions and glass *A* is in the LZS family.

Characterization of all the glass-ceramic specimens was hampered by their extreme electron beam sensitivity. This can be clearly seen in Fig. 4 for the case of a bulk glass-ceramic *D* specimen. In Fig. 4a the microstructure is a randomly oriented distribution of needle-like crystals 0.5–1 μm long and approximately 0.07 μm in diameter. In Fig. 4b the same area is shown 1 min later. Many of the needle crystals have disappeared and those remaining are smaller. In their place spherical regions about 0.1 μm in diameter have appeared. By the time Fig. 4c has been taken, all the needle crystals have been replaced by spheres. Good selected area diffraction (SAD) patterns from the needles proved impossible to obtain because of this instability. Diffraction patterns after this structural transformation had occurred showed a diffuse halo, indicating that the spheres represented a glass-in-glass phase separation.

The one stable crystalline phase in the bulk glass-ceramic *D* sample was the microcrystalline region shown in Fig. 5a. SAD from this region produced the spotty ring pattern shown in Fig. 5b. This is caused by the small size of the crystals in relation to the smallest SAD aperture (approximately 1 μm). Measurements from the pattern were consistent with it being α-quartz. Similar microcrystalline regions were seen in back-thinned coatings of glass-ceramic *A* but not in glass-ceramic *C* coatings.

Fig. 6 shows a region in a glass-ceramic *C* coating. Two phases can be seen, equiaxed crystals 1.5–2 μm in diameter and smaller elongated crystals approximately 0.2 × 0.08 μm in size. The latter were too small for SAD analysis; however diffraction patterns from the larger crystals indicated they were β-spodumene.

3.2. Glass-ceramic/metal interfaces

3.2.1. Copper/glass-ceramic A

The etched cross-section in Fig. 7a shows large acicular crystals dominating the microstructure. Some of

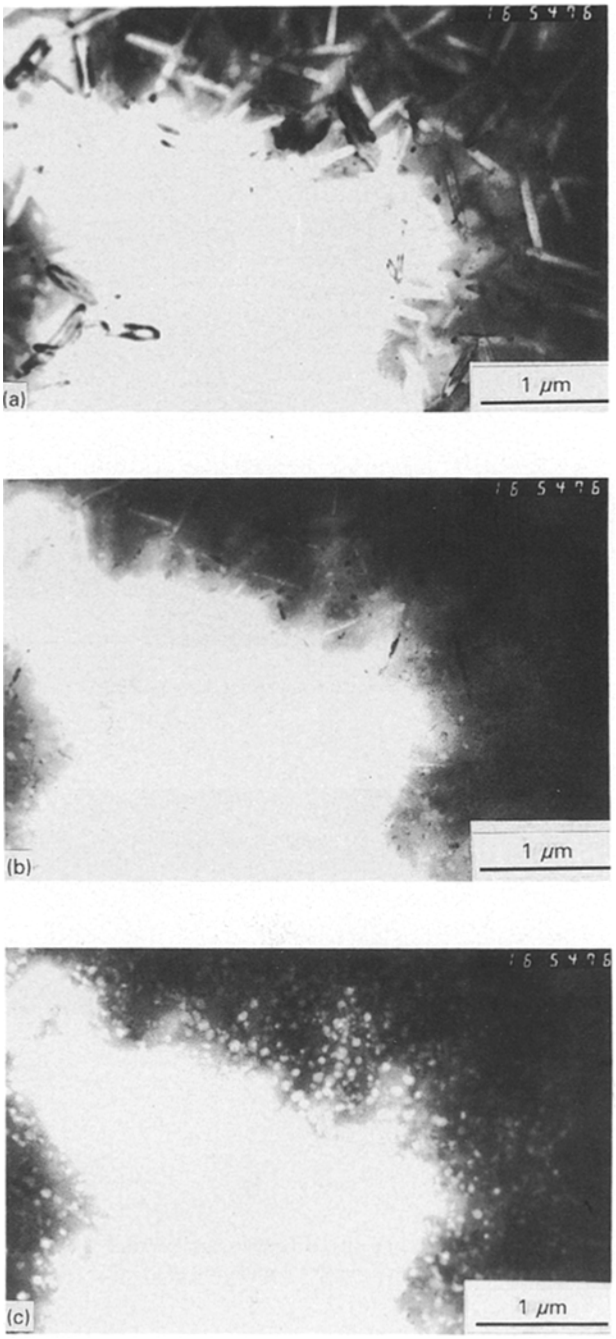

Figure 4 Microstructure of bulk glass-ceramic *D* as a function of time in the electron beam during TEM investigation, showing extreme beam sensitivity: (a) initial exposure to beam, (b) after 3 min, (c) after 10 min.

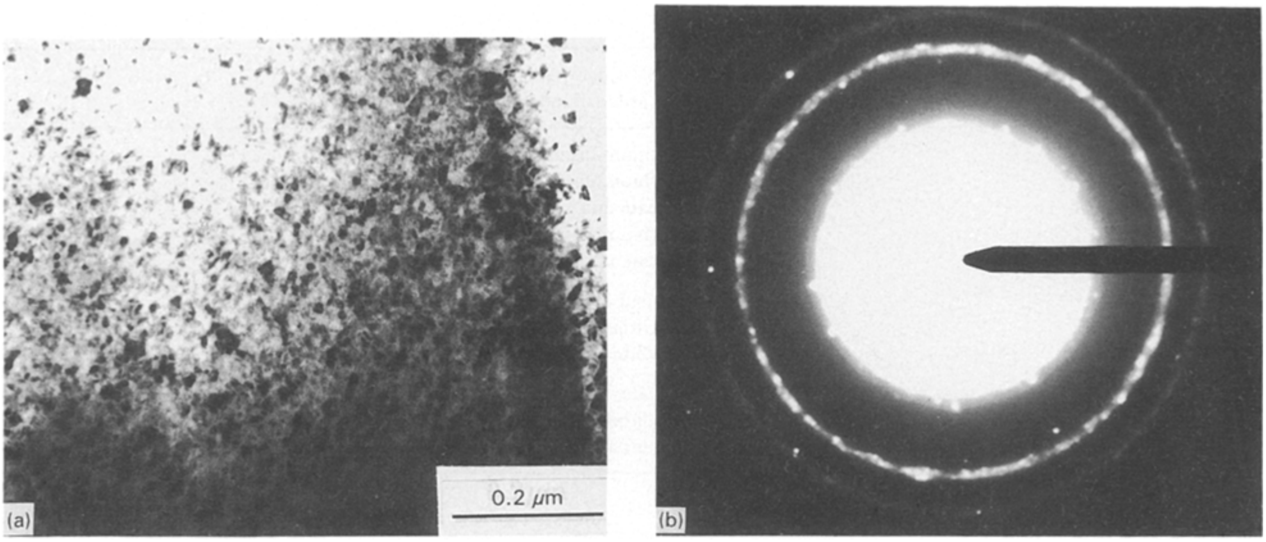

Figure 5 TEM micrographs of bulk glass-ceramic *D*: (a) stable crystalline phase, (b) selected area diffraction pattern from (a). Spotty ring features confirm small grain size.

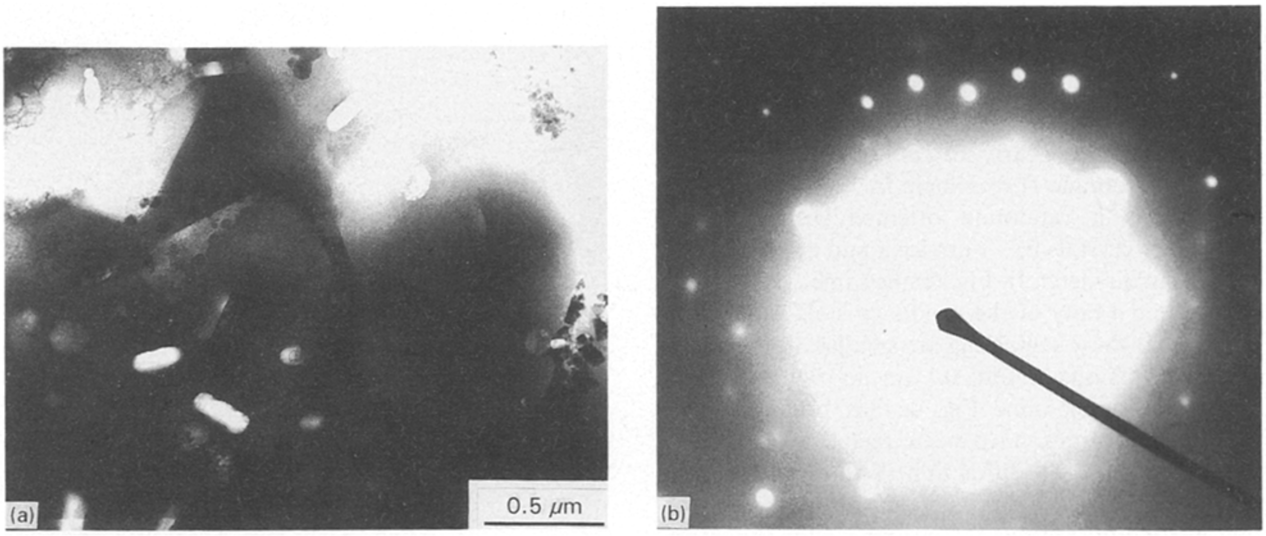

Figure 6 TEM micrograph from a coating of glass-ceramic *C*: (a) very small elongated crystals, (b) selected area diffraction pattern from large crystal in (a).

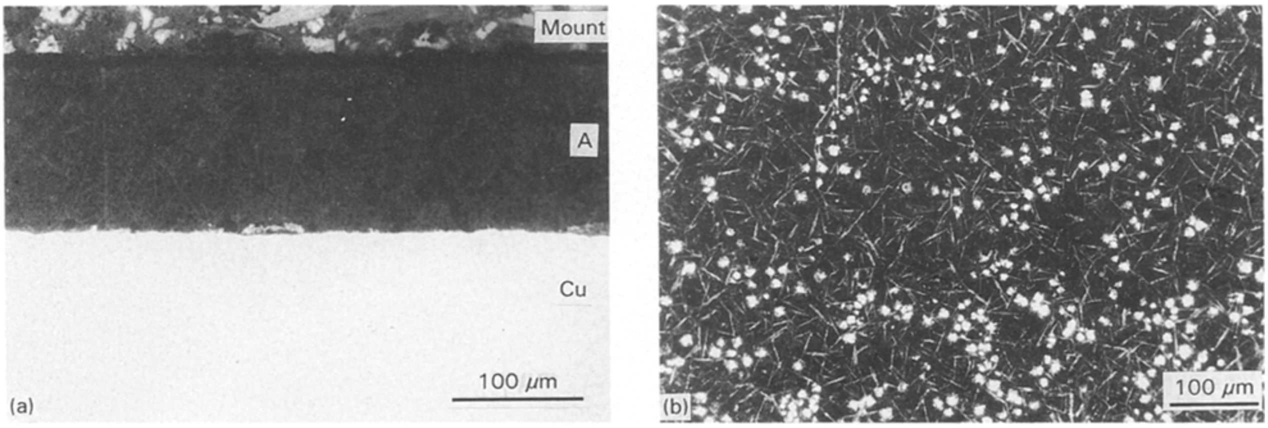

Figure 7 Optical micrographs of copper/glass-ceramic *A* specimens: (a) polished cross-section showing long acicular crystals, (b) glass-ceramic surface showing extensive population of acicular crystals.

these crystals have grown to greater than 100 μm in length and are 1–2 μm in diameter. Equiaxed crystals, 1–2 μm in diameter, are visible between the acicular crystals. It is possible that these may be the acicular crystals viewed perpendicular to their long axis. There are a small number of much larger equiaxed crystals approximately 10 μm in diameter. The acicular crystals show no definite orientation. Adjacent to the interface with the metal are a large number of much shorter acicular crystals $< 25\ \mu m$ in length which appear to be randomly oriented. In Fig. 7b acicular crystals about $30\ \mu m$ in length and $1\ \mu m$ diameter can be seen near the surface of sample 5. There are also reflective, equiaxed crystals of about $10\ \mu m$ diameter in small groups.

Fig. 8a shows a secondary electron image of a copper/glass-ceramic *A* cross-section. There are large needle shaped crystals in the coating, approximately $50\ \mu m$ in length and $1.5\ \mu m$ across, which do not appear to have a preferred orientation. Equiaxed crystals, approximately $1.5–2\ \mu m$ square, could also be seen but these may be cross-sections of the needle crystals. The mean crystallinity of the microstructure is high, in the region of 80–90%. Considerable copper oxide precipitation is visible at the interface. An enlarged image of one precipitate is shown in Fig. 8b. A number of the small needle crystals seem to be in contact with the precipitate, with the oxide precipitate conforming with the ends of the needle crystals. There appears to be an intermediate phase between these precipitates and the copper substrate. This material appears to be glassy and closely follows the surfaces of the metal and the precipitate. Fig. 8c shows a region of direct metal/glass-ceramic contact; needle crystals are seen in contact with the copper on the right of the micrograph. To the left of the crystals is a dark region which may be more of the glassy phase. Fig. 8d shows the microstructure distant from the interface and acicular and blocky crystals $1–2\ \mu m$ square can be seen. These may be two views of the same acicular crystal; however the blocky crystal can sometimes be seen overlying the acicular form and so may represent a distinct phase.

Fig. 9 shows a microprobe trace of composition across the copper/glass-ceramic *A* interface in sample 5. Only the major constituent elements, with the exception of Li, are shown. Elements present in smaller quantities were investigated but they provided little further information. The interfacial region is $3–5\ \mu m$ wide and although there is negligible diffusion from the coating to the substrate, copper has diffused extensively into the glass-ceramic. Copper was present throughout the coating at a background level 3–5%, and in one region approximately $30\ \mu m$ from the interface rose to 30% for $2\ \mu m$ which may indicate the presence of an oxide precipitate sub-surface.

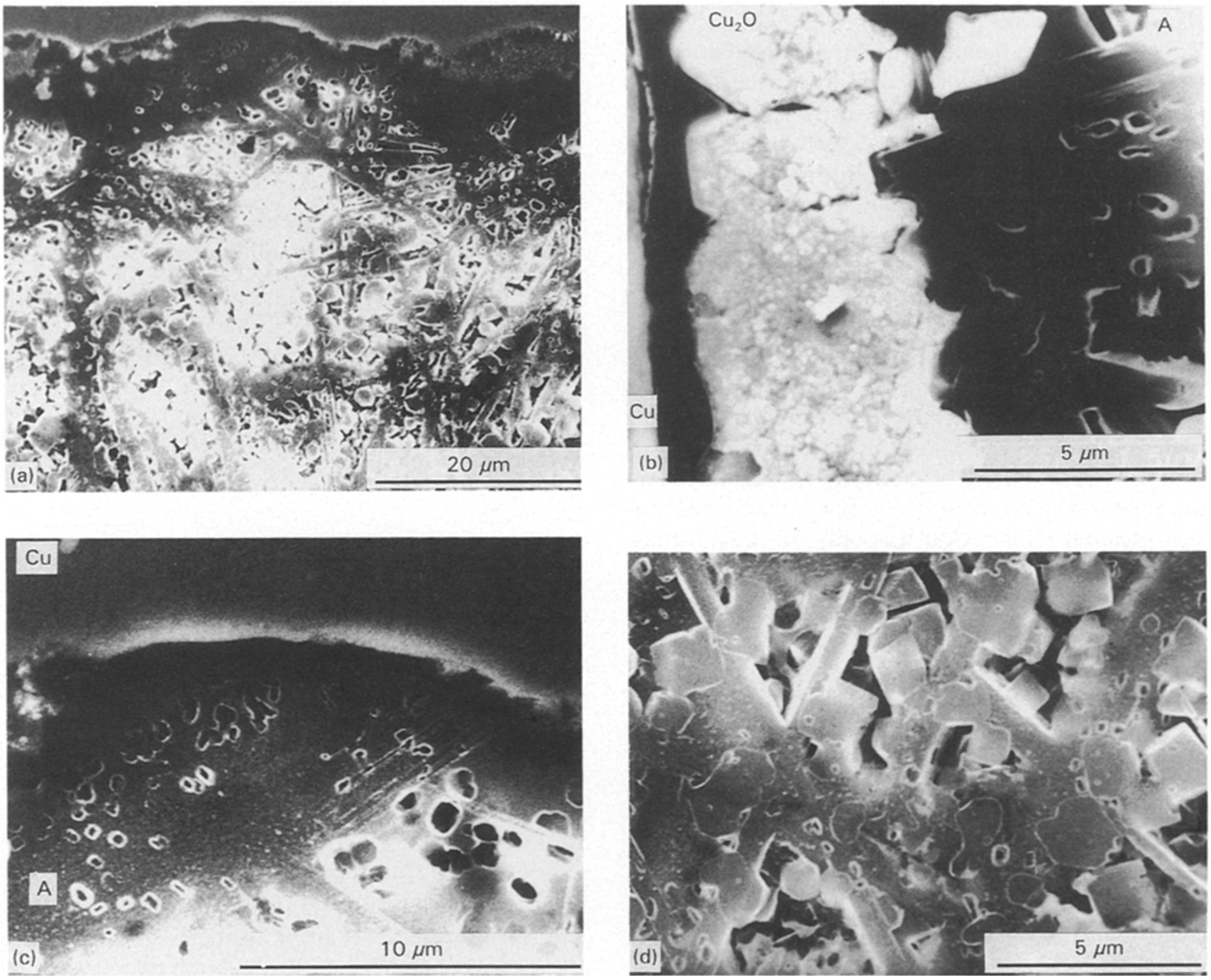

Figure 8 Secondary electron SEM micrographs from polished cross-sections of copper/glass ceramic *A* specimens: (a) glass-ceramic coating showing large acicular crystals; (b) interface between copper and glass-ceramic *A* (a large copper oxide precipitate fills most of the left side of the micrograph); (c) interface between metal and glass-ceramic *A* showing no oxide present; (d) microstructure distant from the interface showing acicular and equiaxed crystals.

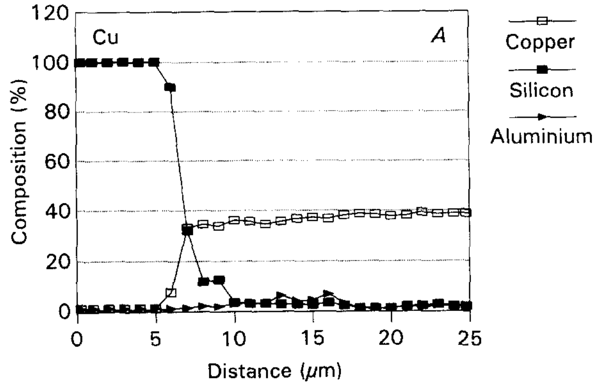

Figure 9 Electron microprobe analysis line scan across the copper/glass-ceramic *A* interface.

3.2.2. *CIC/glass-ceramic A*

The interface here is expected to be chemically similar to that found with copper substrates. Only the residual stress state should be significantly different. Large acicular crystals are found, as with the copper substrate, in Fig. 10a; the orientation of the crystals changes from parallel to almost perpendicular to the interface forming a fan shaped pattern. A high degree of crystallinity is evident. In Fig. 10b the long axes of the crystals are normal to the plane of the image giving the appearance of closely packed equiaxed crystals. There is a change in microstructure about 30 μm from the interface and becomes less clearly defined. There is a dark layer 6–10 μm wide directly adjacent to the interface, which is probably caused by preferential etching of the glass-ceramic in this region.

Fig. 11 shows a microanalytical line scan which crosses a copper oxide precipitate at the metal/glass-ceramic interface. There has been considerable interdiffusion at the oxide/glass-ceramic interface. Between the copper and the copper oxide there is a region enriched in Si and Zn. The line scan leaves a trace on the specimen surface visible in Fig. 10c and marked **P**–Q; this further confirms the susceptibility of these materials to electron beam induced damage. There is a thin dark layer visible between the copper oxide and the copper which probably represents the Si- and Zn-rich material. This region was only 0.8–1.2 μm thick and could not, therefore, be resolved by the microprobe. Thus we do not know whether the region is a distinct phase or a segregation. Fig. 10c also shows the formation of large needle-shaped crystals in the coating. These have formed at angles of 45–90° to the interface with a tendency to converge towards the interface producing fan-like patterns. There is also a region approximately 25 μm thick adjacent to the interface which appears different from the rest of the coating. This may be related to the region of high copper and zinc content about 15 μm from the interface in Fig. 11.

3.2.3. *CIC/glass-ceramic C*

In sample 3 the CIC substrate was pre-oxdized before screen printing the glass slurry. The effect of this is clearly visible in Fig. 12a where a continuous oxide layer about 9 μm thick is visible along the interface. Equiaxed crystals 3–9 μm in diameter can be seen in the glass-ceramic film. In Fig. 12b the microstructure is seen to consist mainly of small equiaxed crystals 0.5–1 μm in diameter and larger crystals approximately 5 μm across. There is little sign of the acicular microstructures so common in the other glass-ceramic

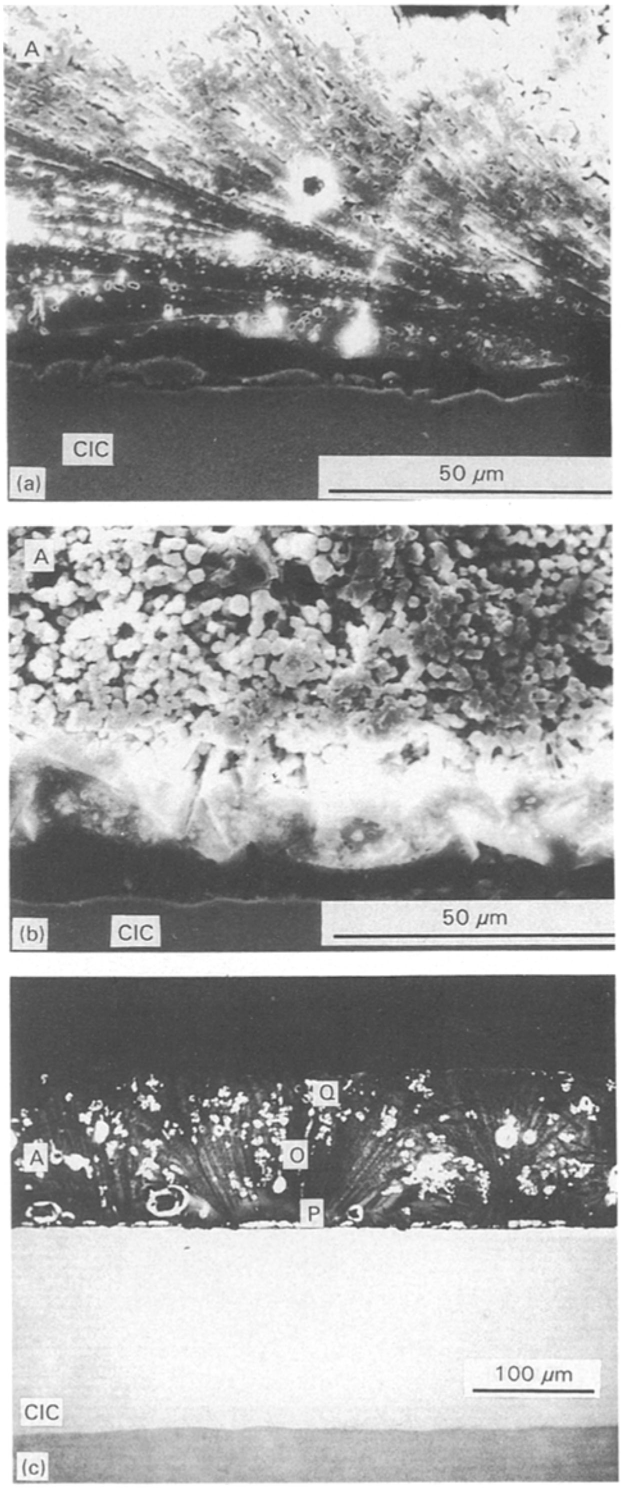

Figure 10 SEM micrographs from polished cross-sections of CIC/glass-ceramic *A* specimens: (a) secondary electron image showing large acicular crystals, (b) secondary electron image showing a change in microstructure through the film thickness, (c) absorbed current image showing elemented contrast and copper oxide islands adjacent to the CIC substrate. The line **P–Q** shows beam damage from a microanalytical line scan.

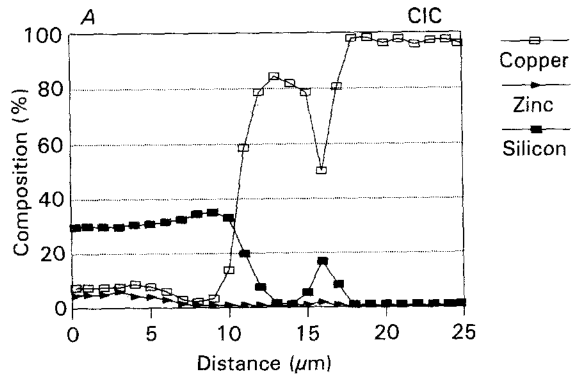

Figure 11 Electron microprobe line scan across the CIC/glass-ceramic *A* interface.

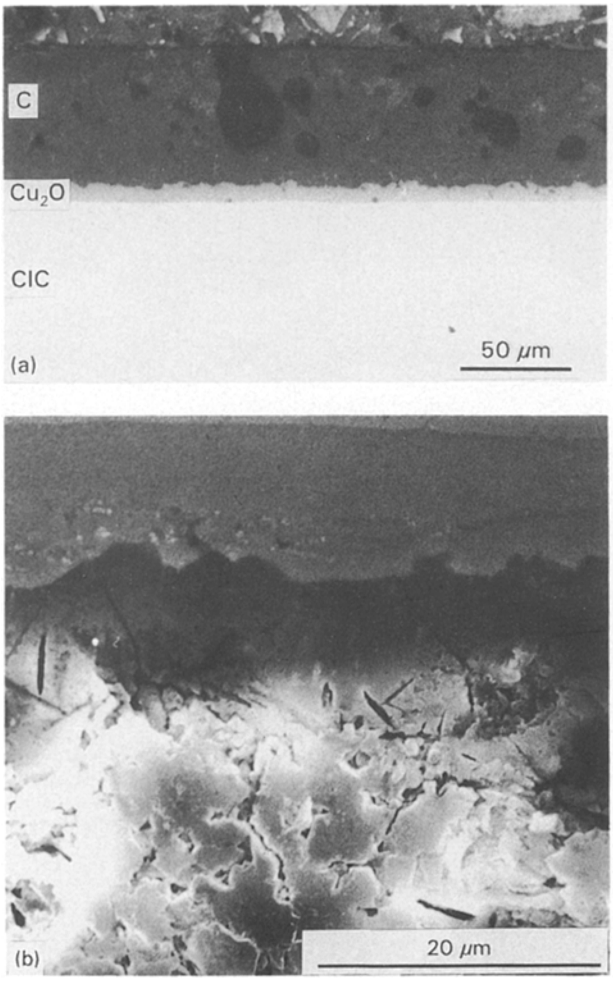

Figure 12 Cross-sections of CIC/glass-ceramic C; (a) optical micrograph showing continuous layer of copper oxide at the metal/glass-ceramic interface, (b) secondary electron SEM image.

coatings. Fig. 13 shows a microanalytical trace across the interface in specimen 3. There is a region approximately 10 μm wide with a very high copper content of 88%. This is a region of Cu_2O corresponding to the red/brown colour of the oxide deposit visible on the rear of the copper substrate. The Cu/Cu_2O interface is less than 1 μm wide, whereas between the glass-ceramic and the oxide an interfacial region of 5 μm width can be seen. This incorporates a region where the Cu content seems anomalously high.

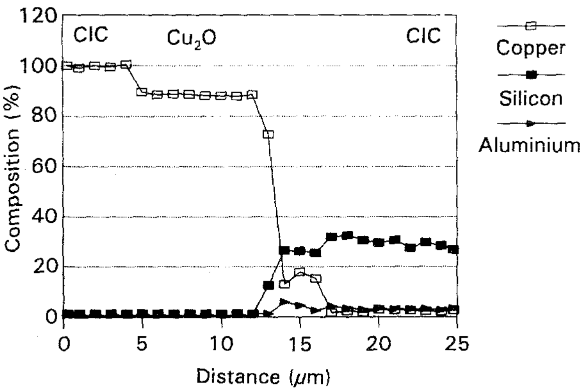

Figure 13 Electron microprobe line scan across the CIC/glass-ceramic *C* interface. Thick Cu_2O layer is clearly visible.

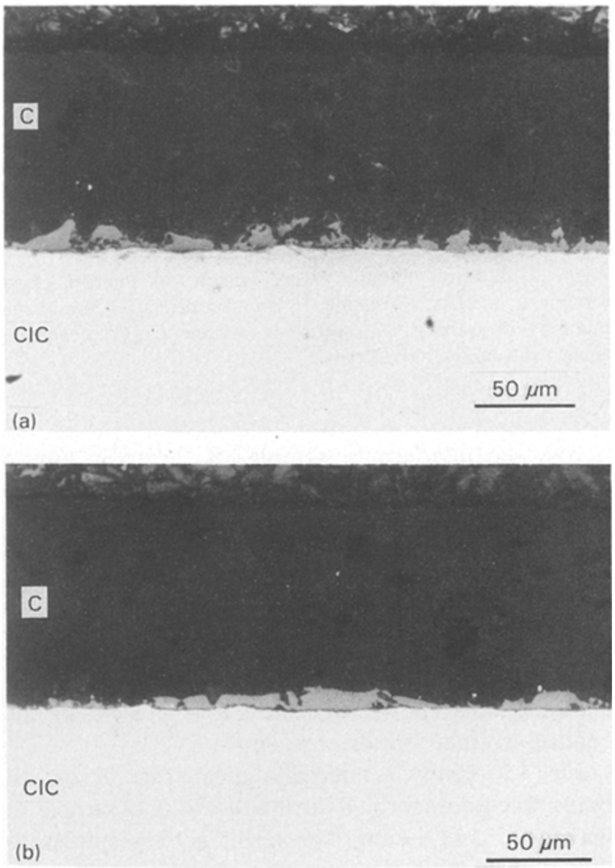

Figure 14 Cross sections of CIC/glass-ceramic *C*: (a) optical micrograph showing extensive but discontinuous copper oxide layer close to the interface (sample 18, pre-oxidized CIC), (b) optical micrograph of sample 13 (not pre-oxidized) also showing copper oxide at the interface.

Figure 14a shows cross-sections through sample 18 which was also pre-oxidized but in this case no continuous oxide layer formed although there is extensive oxide precipitation in the region adjacent to the interface. Even if the specimens were not pre-oxidized, as was the case with sample 13, extensive oxide precipitation in the coating occurs during firing as can be seen in Fig. 14b. Oxide precipitation occurs up to 9 μm within the glass-ceramic film but again does not form a continuous layer. Fig. 15 shows a line trace

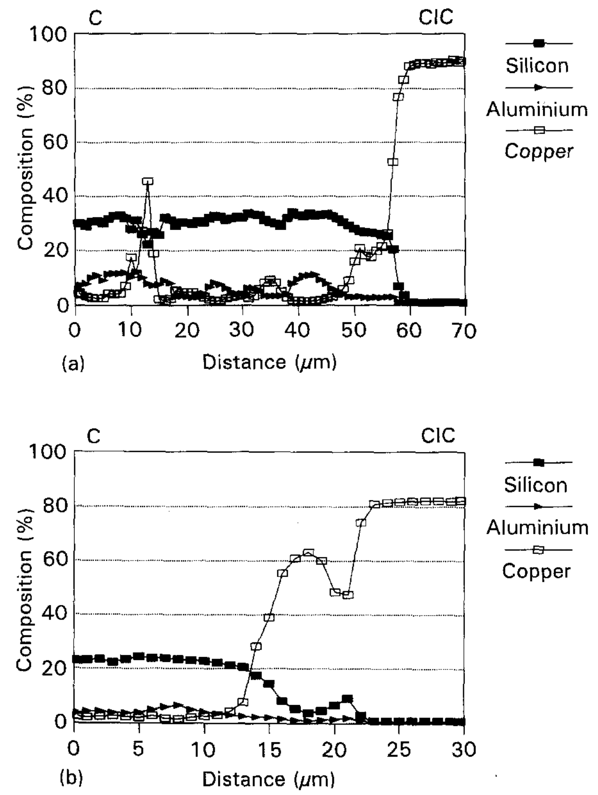

Figure 15 Electron microprobe line scan across the CIC/glass-ceramic *C* interface: (a) sample 18 showing no Cu_2O film at the interface, (b) sample 13 showing a discrete Cu_2O precipitate separated from the interfaces.

across the interface in sample 18. There is now a region about 5 μm wide adjacent to the interface containing approximately 20% Cu and 25% Si. This is clearly not a pure Cu_2O layer as seen in Figs 12 and 13 and either represents another copper-rich phase or the probe sampling a mixture of glass-ceramic and Cu_2O. The Cu content varies markedly across the coating and occasionally achieves quite high concentrations. This shows that the Cu is present in the coating in small but discrete spots.

Fig. 15b shows a microanalytical trace across an oxide precipitate formed during the firing of sample 13 without pre-oxidation. The result is very similar to that shown with glass-ceramic *A* in Fig. 12, i.e. a region of approximately 1 μm between the Cu_2O precipitate and the Cu substrate shows a decreased Cu content and corresponding increases in Si and Al.

3.2.4. CIC/glass-ceramic D

Preferential etching of the interface restricted observation of the CIC/*D* interface. The microstructure in Fig. 16a shows acicular crystals up to 15 × 1 μm in size throughout the coating and particularly in the region adjacent to the interface. Further from the interface equiaxed crystals approximately 2 μm in diameter are visible. At the top of the micrograph another phase approximately 17 × 8 μm in extent can be seen. An enlarged image of an interfacial oxide precipitate is shown in Fig. 16b. The line trace of Fig. 17 crosses a Cu_2O precipitate and again an intermediate region of about 5 μm width exists between the oxide and the glass-ceramic. However in this case there is no increase in the Si or Al content of the material to accompany the decrease in Cu level.

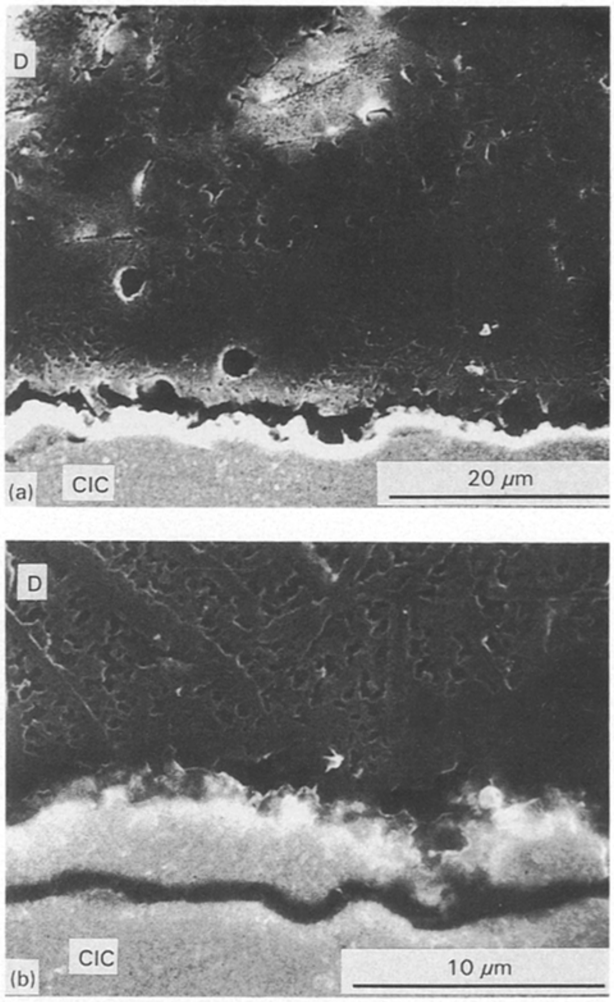

Figure 16 Cross-sections of the CIC/glass-ceramic *D* interface: (a) secondary electron SEM image showing deep etching of the interface, (b) acicular crystals visible in glass-ceramic. Second phase present at the interface.

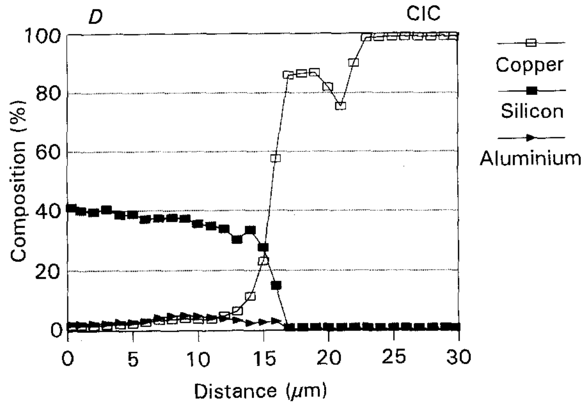

Figure 17 Electron microprobe line scan across the CIC/glass-ceramic D interface showing a Cu_2O precipitate near the interface.

3.4. Adhesion of the glass-ceramic films

The adhesion strengths of these glass-ceramic films to the metal substrates has been measured using a

TABLE IV Ranking order of glass-ceramic to substrate adhesion from a range of adhesion tests [6]

Adhesion test	Ranking order	Range of Results
Pull test	Cu(Ox)/*A* < CIC/*C*, *D* < Cu/*A*	$32 < \sigma < 80$ MPa
Scratch test	CIC(Ox)/*C* < CIC/*C*, *D* < Cu, CIC/*A*	$4 < L_c < 50$ N
Shear test	CIC/*D* < Cu/*A*	$1.8 < \tau < 3.8$ GPa
Indentation test	CIC(Ox)/*C* < CIC/*D* < Cu/*A*	$1.5 < G_c < 2.7$ kJ m^{-2}
Bend test	Only CIC/*A* tested	$3 < G_c < 5$ J m^{-2}

Ox, continuous Cu_2O layer along the copper/glass-ceramic interface.

number of different techniques and reported elsewhere [5, 6]. No absolute quantitative measure of interfacial adhesion could be measured because of various shortfalls in the analyses each of the tests used, all the tests ranked the samples tested in the same order of increasing adhesion test. A summary of these results are presented in Table IV and a general ranking of the relative glass-ceramic film adhesion can be made with the following order of relative adhesion strength

$$(\text{Cu or CIC})\ /A\ >\ \text{CIC}/(C \text{ or } D)\ >\ \text{CIC/Ox}/C$$

where CIC/Ox/*C* indicates a continuous oxide film at the metal/glass-ceramic interface.

4. Discussion

4.1. Crystal phases present in the glass-ceramics

The needle-shaped crystals are probably lithium disilicate. There are a number of reasons for reaching this conclusion. First, it is the only crystalline phase detected known to commonly appear in this form. Second, the only coating in which these crystals were not detected was glass-ceramic *C* which also was the only sample not to show lithium disilicate in its X-ray trace. The instability of the needles under the electron beam in the TEM, which prevented their conclusive identification, is likely to occur if there is Li present which evaporates easily under these conditions. The microcrystalline phase present in the TEM images is probably quartz. This was the only crystalline phase detected in bulk glass-ceramic *D* and in coatings of glass-ceramics *A* and *C*. In thick-film glass-ceramics the large equiaxed crystals 1–9 μm in diameter are probably β-spodumene, which commonly appears in glass-ceramics in this form and because quartz was only detected as a minor phase. The equiaxed crystals in the glass-ceramic *A* coatings could be quartz; however, there were a number of unidentified X-ray peaks in these materials indicating the possible existence of an unknown phase.

It was not possible to directly attribute particular peaks on the DTA curves directly to the appropriate crystalline phases because the DTA samples were too small for reliable X-ray analysis. However, using the other characterization work carried out we can infer that in Fig. 3 the peaks relate to the formation of lithium disilicate and quartz, and that Fig. 4 shows lithium disilicate, β-spodumene and quartz. McMillan *et al.* [3] observed DTA peaks in a Li_2O–SiO_2 glass-ceramic at approximately 600 and 730 °C which corresponded to the crystallization of lithium silicate and quartz respectively. The precise temperature at which a crystalline phase will form depends on a number of factors including firing rate and nucleation sites. In addition it should not be expected that all the crystallization peaks will necessarily correspond to phases found in the fully crystalline material. McMillan *et al.* [3] and Borom *et al.* [4] have reported that the first crystalline phase to appear in a Li_2O–SiO_2 glass-ceramic was lithium metasilicate, which then disappears as the temperature increases. Borom *et al.* believed the metasilicate dissolved into the melt from which the disilicate crystallized, whereas McMillan *et al.* proposed the following reaction

$$2Li_2O.SiO_2 \rightarrow Li_2O.2SiO_2 + Li_2O$$

It must also be noted that it is impossible to say how close these results correspond to crystalline phase development in thick films.

4.2. Glass-ceramic to metal interfaces

Glass-ceramic *A* was coated onto both Cu and CIC substrates. Lithium disilicate and quartz were identified from the X-ray traces, although the presence of other unidentifiable peaks indicated the presence of other, unidentified, crystalline phases. With both substrates 100 μm long and 2 μm in diameter lithium disilicate acicular crystals formed. These were more or less randomly oriented with respect to the interface although the CIC substrate did induce a certain amount of parallel alignment of the crystals. Some smaller equiaxed crystals also formed. At the interface Cu_2O precipitates form and, if the substrate has been pre-oxidized, a continuous Cu_2O layer was sometimes found. Cu diffused throughout the glass-ceramic to a background level of 3–5%. There are occasional Cu-rich areas which suggest that either Cu or Cu_2O precipitates form throughout the glass-ceramic away from the interface. For both substrates there was a thin glassy region between the metal and the Cu_2O precipitates which in the case of the CIC substrates was enriched in Zn and Si. Comparison of Figs 10 and 12 shows a significant influence of the substrate on the crystallized glass-ceramic microstructure. The only difference between the two samples shown will be the state of residual stress. Glass-ceramic *A* was developed to have an expansion match with Cu and thus it will have a much higher level of residual stress when used with CIC. This greater stress state could also explain the preferential etching found at the glass-ceramic/

CIC interface. However it is possible that small differences in the firing cycle between the two batches of specimens may have also had an effect.

Sample 3 was pre-oxidized before coating and a continuous Cu_2O film about 9 μm thick has developed between the copper and the glass-ceramic coating. In this case there is a sharp interface between the Cu and Cu_2O with an interdiffusion zone approximately 5 μm wide between the Cu_2O and the glass-ceramic. However pre-oxidation did not always result in a continuous oxide film as can be seen from sample 18. Indeed firing without preoxidation seemed to produce Cu_2O at the interface in sample 13. In this case a glassy-like layer enriched in Si and Al formed between the Cu and the Cu_2O similar to the glassy layers found with glass-ceramic *A*.

Lithium disilicate, β-spodumene and quartz were all identified in glass-ceramic *D* coatings. Acicular crystals 15 μm long and equiaxed crystals 1–2 μm in diameter were observed. Cu_2O precipitates were seen at the interface and a microprobe trace across one of these noted a drop in Cu concentration between the metal and the oxide. However, in this case, no corresponding increase in Al or Si was detected. In the TEM smaller acicular crystals about 1 μm long were seen but they were highly unstable in the electron beam, preventing phase identification. It is assumed that the instability is related to Li evaporation. After the disappearance of the needle-like phase the resultant microstructure is amorphous with glass in glass separation.

The role of the copper in promoting adhesion of these films appears to be important. The most successful microstructure was one in which the Cu had diffused throughout the glass-ceramic coating to a level of about 1–3%, occasionally reaching high localized concentrations. Near the interface Cu_2O is present and would appear to have precipitated from the matrix rather than grown on the metal because of the presence of a "glassy" phase between the metal and oxide. In the early part of the firing cycle Cu must diffuse into the coating glass. During crystallization we propose that the Cu is rejected, forming Cu_2O precipitates. These are most extensive adjacent to the metal/glass-ceramic interface where the Cu concentration will be highest and there are plentiful nucleation sites. The residual 1–3% Cu in the glass-ceramic is probably in the glassy phase but may be present in smaller concentrations in the crystalline phases. Pre-oxidation of the substrate to provide a continuous Cu_2O film is not beneficial. The influence of the mismatch in thermal expansion coefficient should not be ignored and in cases of poor mismatch the interface tended to etch preferentially and poorer strengths were recorded.

Acknowledgements

The authors would like to thank Graham Partridge of GEC-Alsthom Research Centre for provision of the facilities to make the films and for his advice throughout the project. I.A.A. would also like to thank the SERC for provision of a Research Studentship.

References

1. P. W. MCMILLAN, B. P. HODGSON and G. PARTRIDGE, *Glass Technol.* **7** (1966) 121.
2. G. PARTRIDGE and C. A. ELYARD, *Brit. Ceram. Proc.* **34** (1984) 219.
3. P. W. MCMILLAN, V. PHILIPS and G. PARTRIDGE, *J. Mater. Sci* **1** (1966) 269.
4. M. P. BOROM, A. M. TURKALO and R.H. DOREMUS, *J. Amer. Ceram. Soc.* **58** (1975) 385.
5. I. A. ASHCROFT, D. Phil. thesis, University of Oxford (1991).
6. I. A. ASHCROFT and B. DERBY, *J. Mater. Sci.* **28** (1993) 2989.

Received 9 November 1993
and accepted 3 February 1994